ACS Energy LETTERS

Cite This: ACS Energy Lett. 2019, 4, 1251−1257

http://pubs.acs.org/journal/aelccp

LETTER

High-Loading Composition-Tolerant Co−Mn Spinel Oxides with Performance beyond 1 W/cm^2 in Alkaline Polymer Electrolyte Fuel Cells

Yao Yang,[†,#] Hanqing Peng,[‡,#] Yin Xiong,[†] Qihao Li,[‡] Juntao Lu,[‡] Li Xiao,[‡] Francis J. DiSalvo,[†] Lin Zhuang,*[,‡] and Héctor D. Abruña*[,†]

[†]Department of Chemistry and Chemical Biology, Baker Laboratory, Cornell University, Ithaca, New York 14853, United States

[‡]College of Chemistry and Molecular Sciences, Hubei Key Lab of Electrochemical Power Sources, and Institute for Advanced Studies, Wuhan University, Wuhan 430072, China

Supporting Information

ABSTRACT: Hydrogen fuel cells operated in alkaline media enable the use of abundant nonprecious 3d metal oxides to replace Pt to catalyze the sluggish oxygen reduction reaction (ORR). Herein, we describe Co−Mn spinel oxide electrocatalysts with metal oxide loadings of up to 80 wt % on carbon supports. Despite little variation in ORR activity derived from rotating disk electrode (RDE) measurements, practical membrane electrode assembly (MEA) tests exhibited significant enhancement in performance when loadings increased from 40 to 80 wt %. This was ascribed to the enhanced mass transport through the thin catalyst layer at 80 wt % (<10 μm). This work highlights the importance of incorporating MEA tests, even in early-stage catalyst development. A benchmark peak power density (PPD) of 1.2 W/cm^2 at 2.6 A/cm^2 was achieved using $MnCo_2O_4$ (80 wt %). $CoMn_2O_4$/C also achieved a PPD of 1.1 W/cm^2 under the same conditions, indicating that MEA performance of Co−Mn oxides is generally high and tolerant to compositional variations that may occur in larger-scale production.

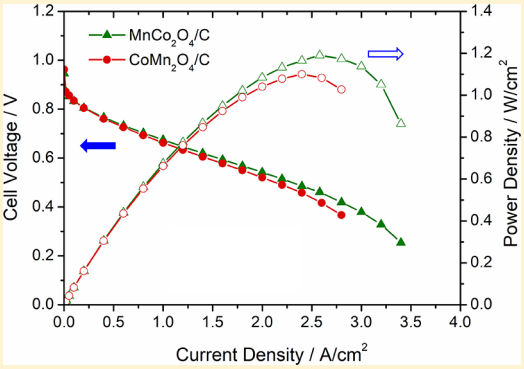

Hydrogen fuel cells have been recognized as a critical renewable energy technology, especially for powering electric vehicles (EVs).[1−3] Despite the tremendous effort in lowering Pt loading in the cathode of proton-exchange membrane fuel cells (PEMFCs), a significant amount of Pt (>0.2 g_{Pt}/kW) is still necessary to provide a power density of >1 W/cm^2 at ≥0.65 V, and the catalyst cost accounts for more than 1/3 of a PEMFC stack cost.[4−8] Alternatively, alkaline polymer electrolyte fuel cells (APEFCs) or anion-exchange membrane fuel cells (AEMFCs), in principle, enable the use of nonprecious metals or metal oxides as stable ORR electrocatalysts.[9,10] A variety of candidates have been reported to show promising ORR activity in alkaline media from rotating disk electrode (RDE) tests, such as precious metal-based alloys,[11−13] N-doped carbons,[14,15] and 3d transition metal oxides.[16−24] However, only few have demonstrated encouraging membrane electrode assembly (MEA) performance in alkaline media.[18,19]

In the development of PEMFCs and APEFCs, the RDE has been widely used in research laboratories to screen electrocatalysts and evaluate their activity/durability. For example, RDE measurements showed rather good quantitative agreement with MEA tests for the benchmark activities of Pt/C in PEMFCs.[3] However, RDE and MEA measurements have significant differences in terms of the test conditions, water management, mass transport mechanism, etc. For instance, although spectacular ORR activity of shape-controlled Pt-based alloy catalysts, up to a factor of 20 relative to Pt/C, was reported from RDE measurements,[25−29] those reports have not translated into realistic MEA results in PEMFCs. After only 1 day of MEA testing, octahedral PtNi catalysts exhibited a loss of their distinct shapes and leached out a significant amount of Ni, contaminating the membrane.[4] In other RDE studies, it was shown that 1−3 atomic layers of Pt on the surface of Pt-based alloys yielded the highest ORR activity under acidic conditions.[8,29−31] However, MEA results in PEMFCs suggested that 4−7 atomic layers of Pt were required to effectively mitigate the transition metal leaching problem while still being thin enough to maintain the lattice strain for enhanced activities.[32−34] In our previous study on

Received: March 19, 2019
Accepted: May 7, 2019
Published: May 7, 2019

DOI: 10.1021/acsenergylett.9b00597
ACS Energy Lett. 2019, 4, 1251−1257

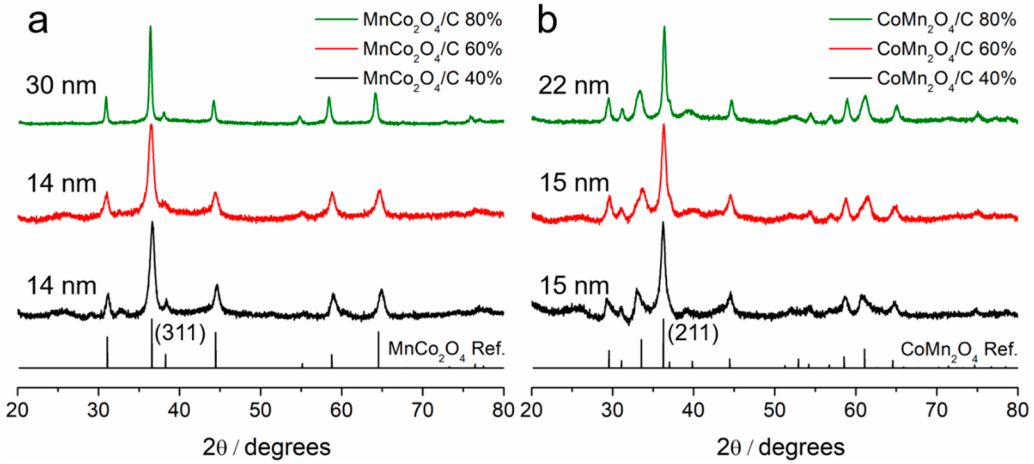

Figure 1. Powder XRD patterns of (a) $MnCo_2O_4$ and (b) $CoMn_2O_4$ NPs with 40, 60, and 80 wt % metal oxide loadings on high-surface-area carbon HSC KB, compared to XRD references of spinel-type $MnCo_2O_4$ and $CoMn_2O_4$. Domain sizes of $MnCo_2O_4$ and $CoMn_2O_4$ NPs are listed on the left side of the XRD patterns.

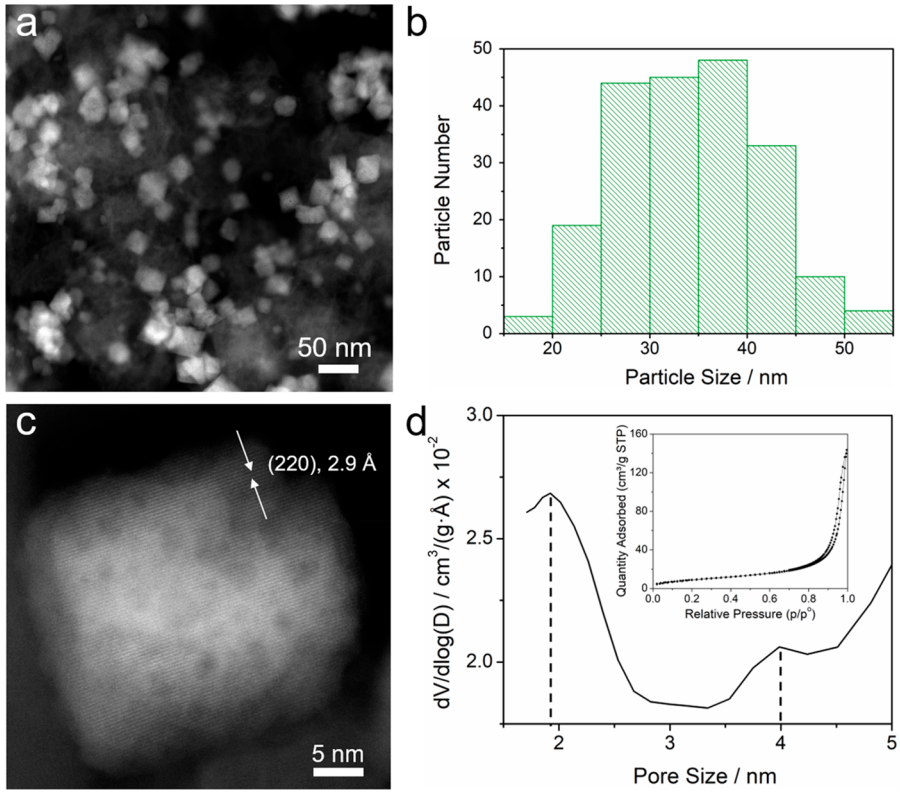

Figure 2. (a) HAADF-STEM image of $MnCo_2O_4$ with 40 wt % metal oxide loading on HSC KB. (b) PSD histogram of $MnCo_2O_4$ NPs. (c) Atomic-scale STEM image of one $MnCo_2O_4$ particle with (220) lattice *d*-spacings (2.9 Å). (d) Pore size distribution of $MnCo_2O_4$ without a carbon support, derived from the N_2 adsorption−desorption isotherm in the inset. The *y*-axis represents the logarithmic differential pore volume distribution, $dV/d\log(D)$, derived from the BJH method. Dashed lines indicate the existence of micropores (1.9 nm) and small mesopores (4.0 nm) in the porous $MnCo_2O_4$ NPs.

$Co_{1.5}Mn_{1.5}O_4$/C for APEFCs, only modest activity was observed from RDE measurements. However, a high power density in MEA measurements, surpassing that of Pt/C at lower relative humidity, was achieved by optimizing the surface composition.[18] The RDE−MEA correlation/discrepancy shows that it is important to include MEA tests in early stage catalyst development, in addition to RDE measurements for catalyst screening.

In this work, we reported on Mn−Co spinel oxide electrocatalysts as the oxygen cathode in practical MEA tests in APEFCs. $MnCo_2O_4$/C (80 wt %) exhibited a peak power density (PPD) of 1.2 W/cm^2, a benchmark value compared to the state-of-art nonprecious cathodes using N-doped carbon (<0.5 W/cm^2)[15,35−38] and 3d metal oxides (0.5−1 W/cm^2).[18,19] With further optimization on MEA components, we predict that Co−Mn oxides could eventually achieve or surpass the performance of precious metal cathodes (e.g., Pt-,

DOI: 10.1021/acsenergylett.9b00597
ACS Energy Lett. 2019, 4, 1251−1257

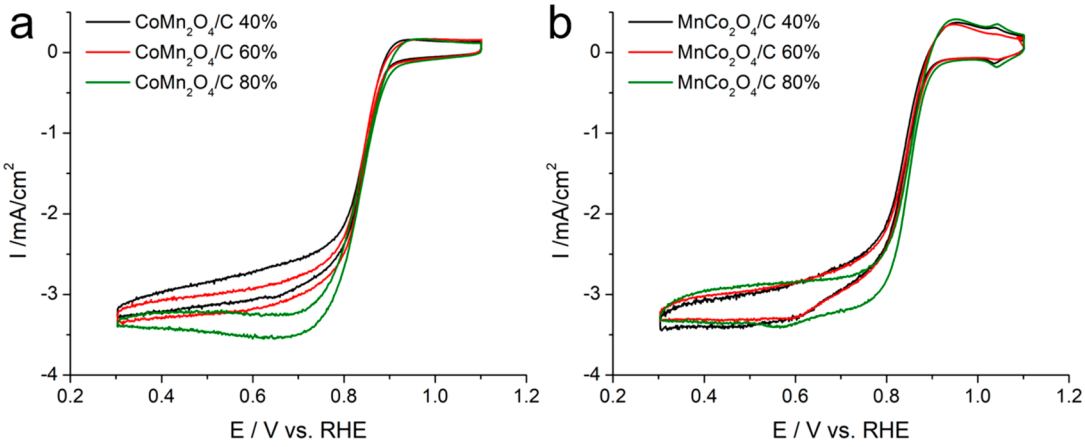

Figure 3. (a) ORR polarization profiles for $MnCo_2O_4$ and (b) $CoMn_2O_4$ with 40, 60, and 80 wt % metal oxide loading on HSC KB in O_2-saturated 1 M KOH at a rotation rate of 1600 rpm and a scan rate of 5 mV/s with a catalyst loading of 0.25 mg/cm^2.

Pd-, and Ag-based catalysts) in APEFCs (1.0−1.5 W/cm^2).[13,14,39−44] The MEA measurements in the literature are summarized in Table S1.

$MnCo_2O_4$ and $CoMn_2O_4$ nanoparticles (NPs) were synthesized using a facile hydrothermal method, using an autoclave, with various metal oxide loadings on carbon supports (Figure S1). Briefly, metal precursors were reacted with ammonium hydroxide to form coordination compounds, which gradually produced metal hydroxide precipitation from the solution through an aging process, at controlled temperatures with selected solvents. Metal hydroxides finally formed spinel metal oxide NPs, supported on high-surface-area carbon Ketjen black (HSC KB) with desired mass loadings. In general, the pH and ethanol/H_2O volume ratio of the solvent control the precipitation rate of metal hydroxides, and therefore, those influence the final metal oxide particle size, morphology, and distribution on the carbon substrate. HSC KB has a mesoporous structure and a large Brunauer−Emmett−Teller (BET) surface area of 900 m^2/g, which was proved to be a better carbon support than the solid carbon, Vulcan XC-72, with a BET surface area of 250 m^2/g in early reports in PEFMCs.[4] Crystal structures of $MnCo_2O_4$/C and $CoMn_2O_4$/C were examined using powder X-ray diffraction (XRD) (Figure 1). $MnCo_2O_4$/C with metal oxide loadings of 40, 60, and 80 wt % all exhibited single-phase cubic spinel structures when compared to the $MnCo_2O_4$ reference (Figure 1a). Such a high loading of 80 wt % has not been reported before for the oxygen cathode in hydrogen fuel cells, although it is a common value used for fabricating the metal oxide cathodes in Li-ion batteries.[45] Average domain sizes of 40, 60, and 80 wt % $MnCo_2O_4$/C were calculated to be 14, 14, and 30 nm, respectively, using the major (311) peak based on the Scherrer equation. Larger domain sizes of 80 wt %, relative to 40 and 60 wt %, suggested that nanocrystals could grow into a larger size at a higher coverage of metal oxides on carbon. As a comparison, $CoMn_2O_4$/C, with various metal oxide loadings, showed a single-phase tetragonal spinel structures due to the strong Jahn−Teller effect of Mn (Figure 1b). The domain size of 80 wt % $CoMn_2O_4$/C was calculated to be 22 nm using the (211) major diffraction peak (PDF # 01-077-0471), which was slightly larger than those at 40 and 60 wt % (15 nm).

The microstructure of Co−Mn NPs supported on HSC KB was examined using aberration-corrected high-angle annular dark-field (HAADF) scanning transmission electron microscopy (STEM). As shown in Figure 2a, $MnCo_2O_4$ NPs (40 wt %) with an octahedral morphology were well-embedded in the carbon matrix. Particle size distribution (PSD) histograms exhibited an average size of 35 nm (Figure 2b), indicating that the majority of the $MnCo_2O_4$ NPs have several subdomains, given the XRD domain size of 14 nm. Atomic-scale STEM images further showed the internal structure of individual $MnCo_2O_4$ NPs. As shown in Figures 2c and S2, single-crystal $MnCo_2O_4$ particles showed lattice *d*-spacings of 2.9 Å, which matched the theoretical value, 2.93 Å, of $MnCo_2O_4$ (220) reflection (PDF # 01-084-0482). Because the STEM image intensity is proportional to the atomic number and relative atomic density, the variation in image contrast suggests the existence of nm-sized pores.

To quantify the porosity of $MnCo_2O_4$ without the influence of the mesoporous carbon substrate, $MnCo_2O_4$ metal oxides were also synthesized without adding HSC KB. The pore size distribution was derived from the N_2 adsorption−desorption isotherm using the Barrett−Joyer−Halenda (BJH) method (Figure 2d). It shows major micropores of 1.9 nm as well as minor small mesopores of 4.0 nm, which are consistent with the pore sizes indicated from previous STEM images (Figures 2c and S2). The specific surface area was estimated to be 34 m^2/g based on the BET analysis (Figure 2d, inset). The electrical conductivity of porous $MnCo_2O_4$, without a carbon support, was estimated to be 19 mS/m when compared to typical values of Si (1.6 mS/m) and amorphous carbon (10^2−10^3 S/m, Figure S3). Given the fact that bulk $MnCo_2O_4$ is an insulator with a band gap of 2.11 eV,[46] the electronic conductivity of $MnCo_2O_4$ NPs may come from crystal defects and small particle sizes, leading to a smaller ohmic resistance for the ORR. $CoMn_2O_4$ NPs (40 wt %) exhibited a similar octahedral morphology with an average particle size of 22 nm, which also indicated the existence of subdomains and nm-sized pores, given the XRD domain size of 15 nm and the STEM image contrast variation (Figure S4).

After thorough structural examination, the Mn−Co spinel oxides with various metal oxide loadings were employed as electrocatalysts for the ORR in alkaline media. ORR polarization profiles were acquired in O_2-saturated 1 M KOH at a rotation rate of 1600 rpm and a scan rate of 5 mV/s with a catalyst loading of 0.25 mg/cm^2. While the metal oxide loadings increased from 40 to 60 and finally 80 wt %, $CoMn_2O_4$/C showed a similar ORR activity with a high half-

DOI: 10.1021/acsenergylett.9b00597
ACS Energy Lett. 2019, 4, 1251−1257

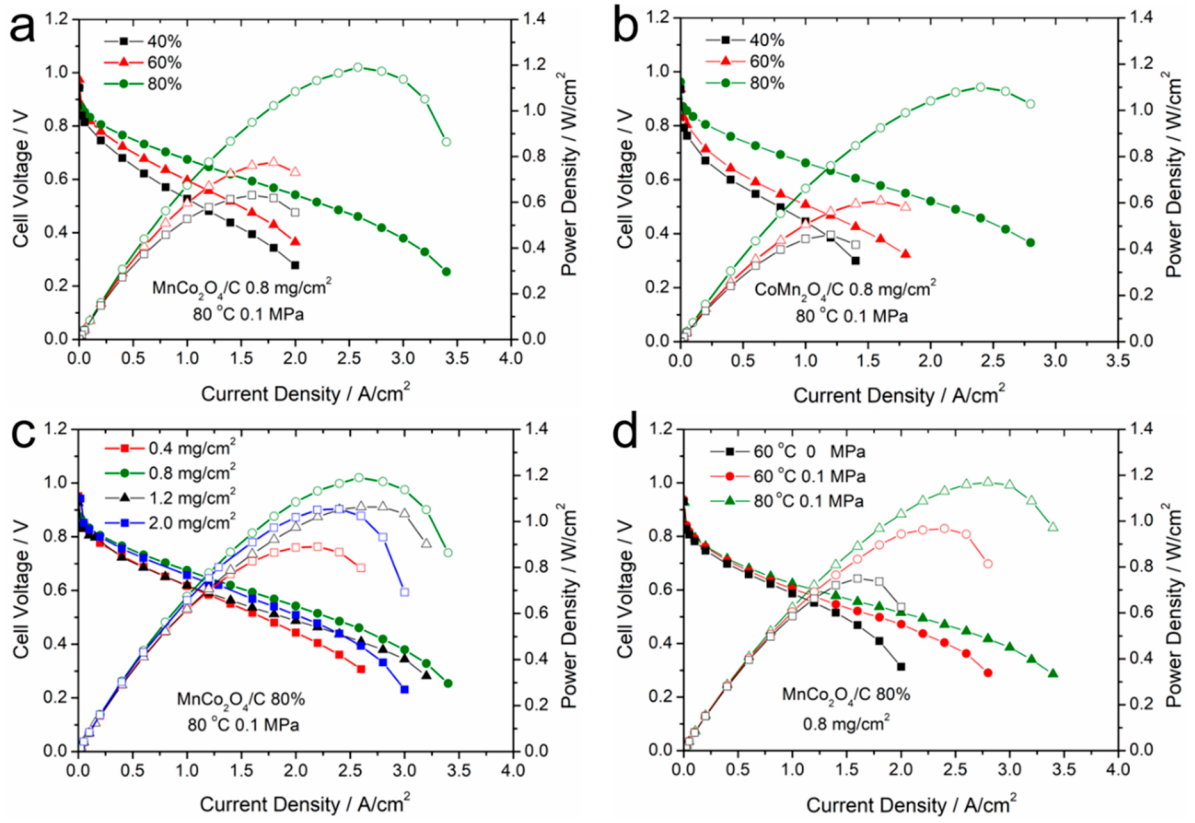

Figure 4. MEA measurements of AEMFCs using Co−Mn spinel oxides in the cathode, 60 wt % PtRu/C (0.4 mg_{PtRu}/cm^2) in the anode, and QAPTT as the alkaline membrane (30 ± 5 μm) and ionomer binder (20 wt % in the catalyst layers). Fully humidified H_2 and O_2 gases were fed into the cell at a flow rate of 1000 mL/min. (a,b) MEA results of $MnCo_2O_4$/C and $CoMn_2O_4$/C with 40, 60, and 80 wt % metal oxide loadings on HSC KB. The catalyst loadings in the cathode were all controlled to be 0.8 $mg_{metal\ oxide}/cm^2$, and the cell operating conditions were 80 °C with 0.1 MPa back-pressure. (c) MEA results of $MnCo_2O_4$/C (80 wt %) with a series of catalyst loadings from 0.4 to 2.0 mg/cm^2 in the cathode with operating conditions of 80 °C and 0.1 MPa back-pressure. (d) MEA results of $MnCo_2O_4$ at different operating conditions (60 or 80 °C; with or without 0.1 MPa back-pressure). Metal oxide loadings on carbon were controlled to be 80 wt %, and catalyst loadings in the cathode were 0.8 $mg_{metal\ oxide}/cm^2$. All of the monotonic cell voltage−current density profiles correspond to the left *y*-axes, while all of the parabolic power density−current density profiles correspond to the right *y*-axes.

wave potential ($E_{1/2}$) of around 0.84 V vs RHE and $\Delta E_{1/2}$ < 3 mV (Figure 3a). Noticeable changes appeared only when the potential was lower than 0.8 V vs the reversible hydrogen electrode (RHE). $CoMn_2O_4$/C with an 80 wt % metal oxide loading achieved the desired diffusion-limited current density at a more positive potential, relative to samples with 60 and 40% loadings. When compared to $CoMn_2O_4$/C, $MnCo_2O_4$ also exhibited similar ORR activity with changes in $E_{1/2}$ less than 5 mV as the metal oxide loading increased from 40 to 80 wt % (Figure 3b). Similar improvement in the high-polarization region was also observed at higher loading despite the small differences between 40 and 60 wt %. The minor redox peaks of $MnCo_2O_4$ at 1.05 V were assigned to monolayer active species on the surface with a highly reversible reaction process (Figure S5). The less smooth changes in the current density at around 0.6 V were ascribed to the influence of $MnCo_2O_4$ reduction peaks at 0.6 V (Figure S5). One may conclude that $MnCo_2O_4$/C and $CoMn_2O_4$/C with high loading (60 and 80 wt %) do not present significant advantages as ORR electrocatalysts, relative to the 40 wt %, which is commonly reported as the metal oxide loading for both RDE and MEA measurements in the literature.[19−24] However, later practical MEA tests of Mn−Co oxides demonstrated the unexpected difference in performance with various metal oxide loadings on carbon (vide infra).

The $H_2−O_2$ cell performance was tested using the quaternary ammonium poly(*N*-methylpiperidine-*co*-*p*-terphenyl) (QAPPT, IEC = 2.58 mmol/g), which was developed early in our group for stable cell operation at 80 °C as the alkaline membrane (thickness of 30 ± 5 μm, Figure S6) and ionomer binder in MEA measurements.[40] PtRu/C (60 wt %, 0.4 mg_{PtRu}/cm^2) was used as the anode catalyst and Mn−Co spinel oxides as the cathode catalyst. The cell was operated at 60 or 80 °C with or without 0.1 MPa back-pressure. Both $CoMn_2O_4$/C and $MnCo_2O_4$ exhibited an impressive enhancement in PPD at 80 °C with 0.1 MPa back-pressure as the metal oxide loading increased from 40 to 60 and 80 wt % (Figure 4a,b). The PPD of $CoMn_2O_4$/C showed a 2-fold enhancement from 0.63 W/cm^2 at 40 wt % to 1.2 W/cm^2 at 80 wt %, while the PPD of $CoMn_2O_4$/C was also boosted from 0.46 W/cm^2 at 40 wt % to 1.1 W/cm^2 at 80 wt % (Figure 4a,b and Tables S2 and S3). To the best of our knowledge, this performance of >1 W/cm^2 at a current density of >2.5 A/cm^2 represents the highest PPD ever achieved by nonprecious ORR electrocatalysts in APEFCs[15,18,19,35−38] and is comparable to the state-of-the-art MEA results of Pt/C (Figure S7). This significant performance enhancement was ascribed to the enhanced mass transport efficiency at higher metal oxide loadings. The catalyst loadings in MEA were fixed at 0.8 $mg_{metal\ oxide}/cm^2$, so that the carbon loadings in MEA were 1.2,

DOI: 10.1021/acsenergylett.9b00597
ACS Energy Lett. 2019, 4, 1251−1257

0.53, and 0.20 mg/cm^2 at metal oxide loadings of 40, 60, and 80 wt %, respectively. SEM images of the cross section showed that the thickness of the catalyst layer decreased from 38 at 40 wt % to 16 at 60 wt % and finally to 8 μm at 80 wt % (Figure S6). A thinner catalyst layer of <10 μm at 80 wt % is more efficient for O_2, H_2O, and OH^- transport, which could more effectively supply reactants, especially for high current densities (>2 A/cm^2), leading to a higher PPD performance.

The impact of the catalyst loading in the cathode was investigated from 0.4 to 2.0 $mg_{metal\ oxide}/cm^2$ (Figure 4c). The cell PPD performance improved significantly from 0.89 to 1.2 W/cm^2 when the catalyst loadings increased from 0.4 to 0.8 mg/cm^2, which was attributed to the increased amount of catalyst active sites. However, further increases in the catalyst loading from 0.8 to 2.0 mg/cm^2 resulted in a noticeable decrease in the PPD from 1.2 to 1.0 W/cm^2. With catalyst loadings higher than 0.8 cm^2, the mass transport limitation became dominant, relative to the increase in the amount of active sites. Different cell operating conditions were also systematically studied, including cell temperatures and operation with or without back-pressure (Figure 4d). The MEA with $MnCo_2O_4$/C (80 wt %) exhibited a PPD enhancement from 0.92 to 1.0 W/cm^2 by applying a 0.1 MPa back-pressure to both H_2 and O_2 and a further PPD increase from 1.0 to 1.2 W/cm^2 when the temperature increased from 60 to 80 °C with a 0.1 MPa back-pressure. $CoMn_2O_4$ showed a similar PPD increase from 0.78 W/cm^2 at 60 °C with no back-pressure to 1.1 W/cm^2 at 80 °C with back-pressure.(Figure S8) This suggests that Co−Mn spinel oxides have excellent temperature-tolerant performance at both 60 and 80 °C, which is critical to maintain the high energy efficiency of fuel cells.[2−4] Few precious[14,40] or nonprecious[18] ORR electrocatalysts can work at such a high temperature of 80 °C at a PPD above 1 W/cm^2. This high power density was attributed to the combination of the high-loading active Co−Mn oxide electrocatalysts and stable QAPPT membrane/ionomers.

In summary, APEFCs with a record peak performance of over 1W/cm^2 power density were achieved for both nonprecious $MnCo_2O_4$/C (1.2 W/cm^2 at 2.6 A/cm^2) and $CoMn_2O_4$/C (1.1 W/cm^2 at 2.4 A/cm^2) with a high metal oxide loading of 80 wt % at 80 °C with 0.1 MPa back-pressure. This work suggests that MEA performance of Co−Mn spinel oxides is generally high even as the Co mole fraction of the cations varies from 2/3 to 1/3 from $MnCo_2O_4$/C to $CoMn_2O_4$/C. Consequently, even when Mn−Co oxide NPs have variations in Mn and Co contents after large-scale synthesis, it will be less challenging to achieve the desired performance in practical fuel cell applications.

■ ASSOCIATED CONTENT

Supporting Information

The Supporting Information is available free of charge on the ACS Publications website at DOI: 10.1021/acsenergylett.9b00597.

Experimental methods, synthesis method, structural characterizations, electrochemical characterizations, MEA tests (PDF)

■ AUTHOR INFORMATION

Corresponding Authors

*E-mail: hda1@cornell.edu.

*E-mail: lzhuang@whu.edu.cn.

ORCID

Yao Yang: 0000-0003-0321-3792
Li Xiao: 0000-0002-6416-3138
Lin Zhuang: 0000-0002-5642-6735
Héctor D. Abruña: 0000-0002-3948-356X

Author Contributions

#Y.Y. and H.P. contributed equally to this work.

Notes

The authors declare no competing financial interest.

■ ACKNOWLEDGMENTS

This work made use of TEM facilities at the Cornell Center for Materials Research (CCMR), which were supported through the National Science Foundation Materials Research Science and Engineering Center (NSF MRSEC) program (DMR-1719875). This work was supported by Dynavolt Renewable Energy Technology Co., LTD. This work was also financially supported by the National Key Research and Development Program of China (2016YFB0101203) and the National Natural Science Foundation of China (91545205, 21633008).

■ REFERENCES

(1) Debe, M. K. Electrocatalyst Approaches and Challenges for Automotive Fuel Cells. *Nature* **2012**, *486*, 43−51.

(2) Xiong, Y.; Yang, Y.; Joress, H.; Padgett, E.; Gupta, U.; Yarlagadda, V.; Agyeman-Budu, D. N.; Huang, X.; Moylan, T. E.; Zeng, R.; Kongkanand, A.; Escobedo, F. A.; Brock, J. D.; DiSalvo, F. J.; Muller, D. A.; Abruña, H. D. Revealing the Atomic Ordering of Binary Intermetallics Using in Situ Heating Techniques at Multilength Scales. *Proc. Natl. Acad. Sci. U. S. A.* **2019**, *116*, 1974−1983.

(3) Gasteiger, H. A.; Kocha, S. S.; Sompalli, B.; Wagner, F. T. Activity Benchmarks and Requirements for Pt, Pt-alloy, and Non-Pt Oxygen Reduction Catalysts for PEMFCs. *Appl. Catal., B* **2005**, *56*, 9−35.

(4) Kongkanand, A.; Mathias, M. The Priority and Challenge of High-Power Performance of Low-Platinum Proton-Exchange Membrane Fuel Cells. *J. Phys. Chem. Lett.* **2016**, *7*, 1127−1137.

(5) Xiong, Y.; Yang, Y.; DiSalvo, F. J.; Abruña, H. D. Pt-Decorated Composition-Tunable Pd−Fe@Pd/C Core−Shell Nanoparticles with Enhanced Electrocatalytic Activity toward the Oxygen Reduction Reaction. *J. Am. Chem. Soc.* **2018**, *140*, 7248−7255.

(6) Wang, D.; Xin, H. L.; Hovden, R.; Wang, H.; Yu, Y.; Muller, D. A.; DiSalvo, F. J.; Abruña, H. D. Structurally Ordered Intermetallic Platinum-Cobalt Core-Shell Nanoparticles with Enhanced Activity and Stability as Oxygen Reduction Electrocatalysts. *Nat. Mater.* **2013**, *12*, 81−87.

(7) Xiong, Y.; Xiao, L.; Yang, Y.; DiSalvo, F. J.; Abruña, H. D. High-Loading Intermetallic Pt_3Co/C Core−Shell Nanoparticles as Enhanced Activity Electrocatalysts toward the Oxygen Reduction Reaction (ORR). *Chem. Mater.* **2018**, *30*, 1532−1539.

(8) Wang, G.; Huang, B.; Xiao, L.; Ren, Z.; Chen, H.; Wang, D.; Abruña, H. D.; Lu, J.; Zhuang, L. Pt Skin on AuCu Intermetallic Substrate: A Strategy to Maximize Pt Utilization for Fuel Cells. *J. Am. Chem. Soc.* **2014**, *136*, 9643−9649.

(9) Lu, S.; Pan, J.; Huang, A.; Zhuang, L.; Lu, J. Alkaline Polymer Electrolyte Fuel Cells Completely Free from Noble Metal Catalysts. *Proc. Natl. Acad. Sci. U. S. A.* **2008**, *105*, 20611−20614.

(10) Varcoe, J. R.; Atanassov, P.; Dekel, D. R.; Herring, A. M.; Hickner, M. A.; Kohl, P. A.; Kucernak, A. R.; Mustain, W. E.; Nijmeijer, K.; Scott, K.; Xu, T.; Zhuang, L. Anion-Exchange Membranes in Electrochemical Energy Systems. *Energy Environ. Sci.* **2014**, *7*, 3135−3191.

(11) Lima, F. H. B.; Zhang, J.; Shao, M. H.; Sasaki, K.; Vukmirovic, M. B.; Ticianelli, E. A.; Adzic, R. R. Catalytic Activity-d-Band Center

DOI: 10.1021/acsenergylett.9b00597
ACS Energy Lett. 2019, 4, 1251−1257

Correlation for the O_2 Reduction Reaction on Platinum in Alkaline Solutions. *J. Phys. Chem. C* **2007**, *111*, 404−410.
(12) Slanac, D. A.; Hardin, W. G.; Johnston, K. P.; Stevenson, K. J. Atomic Ensemble and Electronic Effects in Ag-Rich AgPd Nanoalloy Catalysts for Oxygen Reduction in Alkaline Media. *J. Am. Chem. Soc.* **2012**, *134*, 9812−9819.
(13) Omasta, T. J.; Peng, X.; Miller, H. A.; Vizza, F.; Wang, L.; Varcoe, J. R.; Dekel, D. R.; Mustain, W. E. Beyond 1.0Wcm^{-2} Performance without Platinum: The Beginning of a New Era in Anion Exchange Membrane Fuel Cells. *J. Electrochem. Soc.* **2018**, *165*, J3039−J3044.
(14) Wang, L.; Bellini, M.; Miller, H. A.; Varcoe, J. R. A high conductivity ultrathin anion-exchange membrane with 500+ h alkali stability for use in alkaline membrane fuel cells that can achieve 2 W/cm^2 at 80 °C. *J. Mater. Chem. A* **2018**, *6*, 15404−15412.
(15) Ren, H.; Wang, Y.; Yang, Y.; Tang, X.; Peng, Y.; Peng, H.; Xiao, L.; Lu, J.; Abruña, H. D.; Zhuang, L. Fe/N/C Nanotubes with Atomic Fe Sites: A Highly Active Cathode Catalyst for Alkaline Polymer Electrolyte Fuel Cells. *ACS Catal.* **2017**, *7*, 6485−6492.
(16) Yang, Y.; Wang, Y.; Xiong, Y.; Huang, X.; Shen, L.; Huang, R.; Wang, H.; Pastore, J. P.; Yu, S.-H.; Xiao, L.; Brock, J. D.; Zhuang, L.; Abruña, H. D. In Situ X-ray Absorption Spectroscopy of a Synergistic Co−Mn Oxide Catalyst for the Oxygen Reduction Reaction. *J. Am. Chem. Soc.* **2019**, *141*, 1463−1466.
(17) Xiong, Y.; Yang, Y.; Feng, X.; DiSalvo, F. J.; Abruña, H. D. A Strategy for Increasing the Efficiency of the Oxygen Reduction Reaction in Mn-Doped Cobalt Ferrites. *J. Am. Chem. Soc.* **2019**, *141*, 4412−4421.
(18) Wang, Y.; Yang, Y.; Jia, S.; Wang, X.; Lyu, K.; Peng, Y.; Zheng, H.; Wei, X.; Ren, H.; Xiao, L.; Wang, J.; Muller, D. A.; Abruña, H. D.; Hwang, B. J.; Lu, J.; Zhuang, L. Synergistic Mn-Co Catalyst Outperforms Pt on High-Rate Oxygen Reduction Reaction for Alkaline Polymer Electrolyte Fuel Cells. *Nat. Commun.* **2019**, *10*, 1506.
(19) Peng, X.; Omasta, T. J.; Magliocca, E.; Wang, L.; Varcoe, J. R.; Mustain, W. E. Nitrogen-doped Carbon CoO_x Nanohybrids: The First Precious Metal Free Cathode to Achieve 1.0 W/cm^2 Peak Power and 100 h Life in Anion-Exchange Membrane Fuel Cells. *Angew. Chem., Int. Ed.* **2019**, *58*, 1046−1051.
(20) Liang, Y.; Li, Y.; Wang, H.; Zhou, J.; Wang, J.; Regier, T.; Dai, H. Co_3O_4 Nanocrystals on Graphene as a Synergistic Catalyst for Oxygen Reduction Reaction. *Nat. Mater.* **2011**, *10*, 780−786.
(21) Liang, Y.; Wang, H.; Zhou, J.; Li, Y.; Wang, J.; Regier, T.; Dai, H. Covalent Hybrid of Spinel Manganese−Cobalt Oxide and Graphene as Advanced Oxygen Reduction Electrocatalysts. *J. Am. Chem. Soc.* **2012**, *134*, 3517−3523.
(22) Li, C.; Han, X.; Cheng, F.; Hu, Y.; Chen, C.; Chen, J. Phase and Composition Controllable Synthesis of Cobalt Manganese Spinel Nanoparticles towards Efficient Oxygen Electrocatalysis. *Nat. Commun.* **2015**, *6*, 7345.
(23) Meng, Y.; Song, W.; Huang, H.; Ren, Z.; Chen, S.; Suib, S. Structure−Property Relationship of Bifunctional MnO_2 Nanostructures: Highly Efficient, Ultra-Stable Electrochemical Water Oxidation and Oxygen Reduction Reaction Catalysts Identified in Alkaline Media. *J. Am. Chem. Soc.* **2014**, *136*, 11452−11464.
(24) Indra, A.; Menezes, P.; Sahraie, N.; Bergmann, A.; Das, C.; Tallarida, M.; Schmeißer, D.; Strasser, P.; Driess, M. Unification of Catalytic Water Oxidation and Oxygen Reduction Reactions: Amorphous Beat Crystalline Cobalt Iron Oxides. *J. Am. Chem. Soc.* **2014**, *136*, 17530−17536.
(25) Wu, J.; Zhang, J.; Peng, Z.; Yang, S.; Wagner, F. T.; Yang, H. Truncated Octahedral Pt3Ni Oxygen Reduction Reaction Electrocatalysts. *J. Am. Chem. Soc.* **2010**, *132*, 4984−4985.
(26) Carpenter, M. K.; Moylan, T. E.; Kukreja, R. S.; Atwan, M. H.; Tessema, M. M. Solvothermal Synthesis of Platinum Alloy Nanoparticles for Oxygen Reduction Electrocatalysis. *J. Am. Chem. Soc.* **2012**, *134*, 8535−8542.
(27) Gan, L.; Cui, C.; Heggen, M.; Dionigi, F.; Rudi, S.; Strasser, P. Element-Specific Anisotropic Growth of Shaped Platinum Alloy Nanocrystals. *Science* **2014**, *346*, 1502−1506.
(28) Chen, C.; Kang, Y.; Huo, Z.; Zhu, Z.; Huang, W.; Xin, H. L.; Snyder, J. D.; Li, D.; Herron, J. A.; Mavrikakis, M.; et al. Highly Crystalline Multimetallic Nanoframes with Three-Dimensional Electrocatalytic Surfaces. *Science* **2014**, *343*, 1339−1343.
(29) Huang, X.; Zhao, Z.; Cao, L.; Chen, Y.; Zhu, E.; Lin, Z.; Li, M.; Yan, A.; Zettl, A.; Wang, Y. M.; et al. High-Performance Transition Metal−doped Pt_3Ni Octahedra for Oxygen Reduction Reaction. *Science* **2015**, *348*, 1230−1234.
(30) Strasser, P.; Koh, S.; Anniyev, T.; Greeley, J.; More, K.; Yu, C.; Liu, Z.; Kaya, S.; Nordlund, D.; Ogasawara, H.; Toney, M. F.; Nilsson, A. Lattice-Strain Control of the Activity in Dealloyed Core-Shell Fuel Cell Catalysts. *Nat. Chem.* **2010**, *2*, 454−460.
(31) Wang, C.; Chi, M.; Li, D.; Strmcnik, D.; Van Der Vliet, D.; Wang, G.; Komanicky, V.; Chang, K. C.; Paulikas, A. P.; Tripkovic, D.; Pearson, J.; More, K. L.; Markovic, N. M.; Stamenkovic, V. R. Design and Synthesis of Bimetallic Electrocatalyst with Multilayered Pt-Skin Surfaces. *J. Am. Chem. Soc.* **2011**, *133*, 14396−14403.
(32) Caldwell, K. M.; Ramaker, D. E.; Jia, Q.; Mukerjee, S.; Ziegelbauer, J. M.; Kukreja, R. S.; Kongkanand, A. Spectroscopic in Situ Measurements of the Relative Pt Skin Thicknesses and Porosities of Dealloyed PtMn (Ni, Co) Electrocatalysts. *J. Phys. Chem. C* **2015**, *119*, 757−765.
(33) Han, B.; Carlton, C. E.; Kongkanand, A.; Kukreja, R. S.; Theobald, B. R.; Gan, L.; O'Malley, R.; Strasser, P.; Wagner, F. T.; Shao-Horn, Y. Record Activity and Stability of Dealloyed Bimetallic Catalysts for Proton Exchange Membrane Fuel Cells. *Energy Environ. Sci.* **2015**, *8*, 258−266.
(34) Jia, Q.; Li, J.; Caldwell, K.; Ramaker, D. E.; Ziegelbauer, J. M.; Kukreja, R. S.; Kongkanand, A.; Mukerjee, S. Circumventing Metal Dissolution-Induced Degradation of Pt-Alloy Catalysts in Proton Exchange Membrane Fuel Cells: Revealing the Asymmetric Volcano Nature of Redox Catalysis. *ACS Catal.* **2016**, *6*, 928−938.
(35) Lu, Y.; Wang, L.; Preuß, K.; Qiao, M.; Titirici, M.; Varcoe, J.; Cai, Q. Halloysite-Derived Nitrogen Doped Carbon Electrocatalysts for Anion Exchange Membrane Fuel Cells. *J. Power Sources* **2017**, *372*, 82−90.
(36) Hossen, M.; Artyushkova, K.; Atanassov, P.; Serov, A. Synthesis and Characterization of High Performing Fe-N-C Catalyst for Oxygen Reduction Reaction (ORR) in Alkaline Exchange Membrane Fuel Cells. *J. Power Sources* **2018**, *375*, 214−221.
(37) Sa, Y.; Seo, D.; Woo, J.; Lim, J.; Cheon, J.; Yang, S.; Lee, J.; Kang, D.; Shin, T.; Shin, H.; et al. A General Approach to Preferential Formation of Active Fe−Nx Sites in Fe−N/C Electrocatalysts for Efficient Oxygen Reduction Reaction. *J. Am. Chem. Soc.* **2016**, *138*, 15046−15056.
(38) Kim, O.; Cho, Y.; Chung, D.; Kim, M.; Yoo, J.; Park, J.; Choe, H.; Sung, Y. Facile And Gram-Scale Synthesis Of Metal-Free Catalysts: Toward Realistic Applications For Fuel Cells. *Sci. Rep.* **2015**, *5*, 8376.
(39) Wang, Y.; Wang, G.; Li, G.; Huang, B.; Pan, J.; Liu, Q.; Han, J.; Xiao, L.; Lu, J.; Zhuang, L. Pt−Ru Catalyzed Hydrogen Oxidation in Alkaline Media: Oxophilic Effect or Electronic Effect? *Energy Environ. Sci.* **2015**, *8*, 177−181.
(40) Peng, H.; Li, Q.; Hu, M.; Xiao, L.; Lu, J.; Zhuang, L. Alkaline Polymer Electrolyte Fuel Cells Stably Working at 80 °C. *J. Power Sources* **2018**, *390*, 165−167.
(41) Wang, L.; Brink, J.; Liu, Y.; Herring, A.; Ponce-González, J.; Whelligan, D.; Varcoe, J. Non-Fluorinated Pre-Irradiation-Grafted (Peroxidated) LDPE-Based Anion-Exchange Membranes with High Performance And Stability. *Energy Environ. Sci.* **2017**, *10*, 2154−2167.
(42) Maurya, S.; Noh, S.; Matanovic, I.; Park, E.; Narvaez Villarrubia, C.; Martinez, U.; Han, J.; Bae, C.; Kim, Y. Rational Design of Polyaromatic Ionomers for Alkaline Membrane Fuel Cells with > 1 W cm^{-2} Power Density. *Energy Environ. Sci.* **2018**, *11*, 3283−3291.

DOI: 10.1021/acsenergylett.9b00597
ACS Energy Lett. 2019, 4, 1251−1257

(43) Wang, L.; Brink, J.; Varcoe, J. The First Anion-Exchange Membrane Fuel Cell to Exceed 1 W cm^{-2} at 70 °C with a Non-Pt-Group (O_2) Cathode. *Chem. Commun.* **2017**, *53*, 11771−11773.
(44) Li, Q.; Peng, H.; Wang, Y.; Xiao, L.; Lu, J.; Zhuang, L. The comparability of Pt to Pt-Ru in Catalyzing the Hydrogen Oxidation Reaction for Alkaline Polymer Electrolyte Fuel Cells Operated at 80 °C. *Angew. Chem., Int. Ed.* **2019**, *58*, 1442−1446.
(45) Ren, D.; Shen, Y.; Yang, Y.; Shen, L.; Levin, B. D. A.; Yu, Y.; Muller, D. A.; Abruña, H. D. Systematic Optimization of Battery Materials: Key Parameter Optimization for the Scalable Synthesis of Uniform, High-Energy, and High Stability $LiNi_{0.6}Mn_{0.2}Co_{0.2}O_2$ Cathode Material for Lithium-Ion Batteries. *ACS Appl. Mater. Interfaces* **2017**, *9* (41), 35811−35819.
(46) Shibli, S. M. A.; Arun, P. S.; Raj, A. V. Exploration of Octahedrally Shapes $MnCo_2O_4$ Catalyst Particles for Visible Light Driven Photocatalytic Water Splitting Reaction. *RSC Adv.* **2015**, *5*, 19393−19399.

DOI: 10.1021/acsenergylett.9b00597
ACS Energy Lett. 2019, 4, 1251−1257